



Impact Dynamics of Boulder-Enriched Debris Flow on a Rigid Barrier

Charles W. W. Ng, F.ASCE¹; Haiming Liu²; Clarence E. Choi³; Julian S. H. Kwan⁴; and W. K. Pun⁵

Abstract: Boulders entrained in debris flow induce high impact forces on a rigid barrier. In current design practice, the concentrated load from boulders is estimated using the Hertz equation with a load reduction factor (K_c). Separately, the distributed load from the debris is estimated using the hydrodynamic equation. The existing design practice is simply adding the estimated loads using the two equations. The interaction between debris flow and boulders during the impact process is neglected. In this study, physical tests were conducted using a newly developed 28-m-long flume to shed light on the impact dynamics of debris flows with and without boulders on an instrumented rigid barrier. Contrary to existing design practice in which the boulder and debris impact loads are added together, the debris provided a cushioning effect to attenuate the impact force of the boulders. This cushioning effect was governed by a reflection wave with a length scale L_R/d (where d = boulder diameter), which serves to cushion thickness on impact. L_R/d from 0.4 to 2.0 can reduce the impact load by up to 80% compared with existing design practice ($K_c = 0.1$). DOI: 10.1061/(ASCE)GT.1943-5606.0002485. © 2021 American Society of Civil Engineers.

Author keywords: Debris flows; Boulders; Boulder-enriched flows; Impact; Rigid barrier; Physical modeling.

Introduction

Concentrated impact loads induced by boulders entrained in debris flows are crucial when designing rigid barriers (Hung et al. 1984; Zeng et al. 2015; Ng et al. 2016, 2018; Choi et al. 2016; Lam et al. 2018). Design guidelines generally neglect the interaction between debris flow and boulders. The distributed load from the debris flow is simply added to the concentrated loads from the boulders (Hung et al. 1984; NILIM 2007; Kwan 2012). However, in reality, the viscous forces exerted by the debris flow on boulders may play an integral role in the total impact load.

A literature review on existing approaches to estimate the impact force induced by debris flow and boulders is carried out to reveal the current knowledge gap in predicting the impact force exerted by boulder-enriched debris flows. A hydrodynamic approach (Hübl et al. 2009; Armanini et al. 2011), which is based

on the conservation of momentum, is most widely used to estimate the distributed load induced by debris flow:

$$F = \alpha \rho v^2 h w \quad (1)$$

where α = pressure coefficient; ρ (kg/m^3) = flow density; v (m/s) = flow velocity; h (m) = flow depth; and w (m) = channel width. To account for the simplifications and assumptions in Eq. (1), design guidelines often prescribe higher values of α to Eq. (1) for design robustness. For example, Kwan (2012) recommends an α of 2.5 for the design of rigid barriers to consider hard and large inclusions in the debris flow.

Eq. (1) treats a complex debris flow mixture as an equivalent fluid (Hung 1995), meaning that the distinction between boulders and debris flow is not explicitly made. Because boulders induce concentrated impact loads over a tiny contact area, appropriate mechanics are needed to describe the involved contact between a sphere and a plane. To achieve this, the elastic Hertz equation may be used to estimate the impact load, F_b , induced by a boulder (VanDine 1996; SWCB 2005; Kwan 2012) as follows:

$$F_b = K_c n a^{1.5} \quad (2)$$

$$n = \frac{4r_b^{0.5}}{3\pi(k_b + k_B)} \quad (3)$$

$$a = \left(\frac{5m_b v_b^2}{4n} \right)^{0.4} \quad (4)$$

$$k_b = \frac{1 - \mu_b^2}{\pi E_b} \quad (5)$$

$$k_B = \frac{1 - \mu_B^2}{\pi E_B} \quad (6)$$

where K_c = load reduction factor, which is recommended to be 0.1 to compensate for plastic deformation during impact (Hung et al. 1984; Lo 2000; Sun et al. 2005; Kwan 2012). The variables r , m , v ,

¹Chair Professor, Dept. of Civil and Environmental Engineering, The Hong Kong Univ. of Science and Technology, Hong Kong SAR 999077, China.

²Postdoctoral Fellow, Dept. of Civil and Environmental Engineering, The Hong Kong Univ. of Science and Technology, Hong Kong SAR 999077, China (corresponding author). ORCID: <https://orcid.org/0000-0003-1235-6058>. Email: hliubc@connect.ust.hk

³Assistant Professor, Dept. of Civil Engineering, The Univ. of Hong Kong, Hong Kong SAR 999077, China; The Univ. of Hong Kong, Shenzhen Institute of Research and Innovation, Nanshan, Shenzhen 518057, China.

⁴Chief Geotechnical Engineer, Geotechnical Engineering Office, Dept. of Civil Engineering and Development, Hong Kong SAR 999077, China.

⁵Head, Geotechnical Engineering Office, Dept. of Civil Engineering and Development, Hong Kong SAR 999077, China.

Note. This manuscript was submitted on February 3, 2020; approved on November 12, 2020; published online on January 13, 2021. Discussion period open until June 13, 2021; separate discussions must be submitted for individual papers. This paper is part of the *Journal of Geotechnical and Geoenvironmental Engineering*, © ASCE, ISSN 1090-0241.

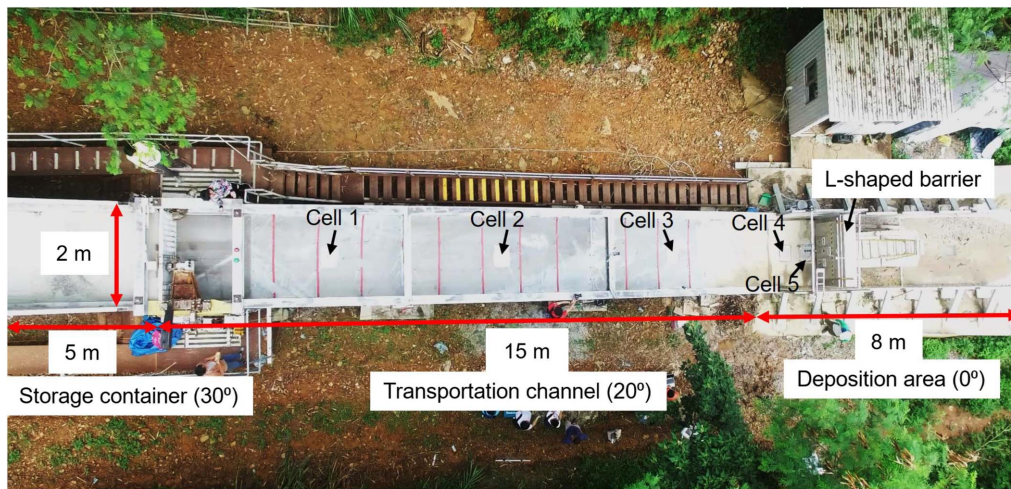


Fig. 1. Plan view of flume facility.

μ , and E are radius (m), mass (kg), impact velocity (m/s), Poisson's ratio, and elastic modulus (Pa), respectively. Subscripts "b" and "B" correspond to the boulder and barrier, respectively.

Song et al. (2018) carried out two series of centrifuge tests to study the impact behavior of idealized dry monodisperse boulder flows with and without sand on a rigid barrier. The prototype diameter of the boulders varied from 70 to 870 mm. Their experimental findings indicated that, as the size of the boulders increased, transient impulses generated by these boulders governed the overall design load. Moreover, it was reported that if Eq. (1) is used to estimate the boulder impact force, then an α of 2.5 can be used to safely determine the impact force for boulders with a diameter up to 0.6 times the flow depth before impact. However, their experiments were conducted using dry granular flows, which are fundamentally different compared with debris flows. For debris flows, both the solid and fluid phases play integral roles in regulating the mesoscopic and macroscopic flow dynamics (Iverson 2015; Ng et al. 2017; Song et al. 2017; Zhou et al. 2018; Song et al. 2018). More importantly, the inertial and static fluid stresses

(Alexander and Cooker 2016) that transport boulders for debris flow are fundamentally different compared with that of dry granular flow.

In this study, boulder flows and debris flows with and without boulders were modeled to investigate the impact mechanisms of boulder-enriched debris flow on a rigid barrier using a newly developed 28-m-long flume model. Impact characteristics for different flow compositions and the effects of debris flow cushioning on boulder impact are examined.

Twenty-Eight-Meter-Long Flume Modeling

Fig. 1 indicates a plan view of the flume model and instrumentation used in this study. The channel has a total length of 28 m and a width and depth of 2 m and 1 m, respectively. The storage tank has a maximum volume of 10 m³. The tank occupies the upper 5 m of the channel, which is inclined at 30°. Just downstream from the storage tank is a 15-m-long channel section that is inclined at 20°. At the end of the inclined channel is an 8-m-long horizontal channel section. A mechanical arm controlled using an electric motor was used to retain and release the dual gates.

An L-shaped reinforced concrete barrier (Fig. 2) was constructed and positioned at the mouth of the inclined section of the channel. The barrier has a height, width, and thickness of 1.8 m, 1.9 m, and 0.3 m, respectively. Four load cells were sandwiched between a stainless-steel force plate and the reinforced concrete barrier to measure the impact load. The stainless-steel plate has a height, width, and thickness of 1,480 mm, 1,900 mm, and 20 mm, respectively. The barrier weighed a total of 4.5 t and was constructed on a 100-mm-thick layer of compacted soil. At the base of the L-shaped barrier, two instrumentation cells (subsequently discussed) were installed to measure the debris flow properties.

Instrumentation

Fig. 3 indicates a typical instrumentation cell installed at the base of the flume to obtain measurements of the model debris flow. The frame of the instrumentation cell was constructed using stainless steel [Fig. 3(a)]. At the top of the frame was a circular opening for a polyvinyl chloride (PVC) plate with a diameter of 0.32 m to transfer loading to a load cell, which was used to measure the basal stresses induced by the debris flow. The load cell rested

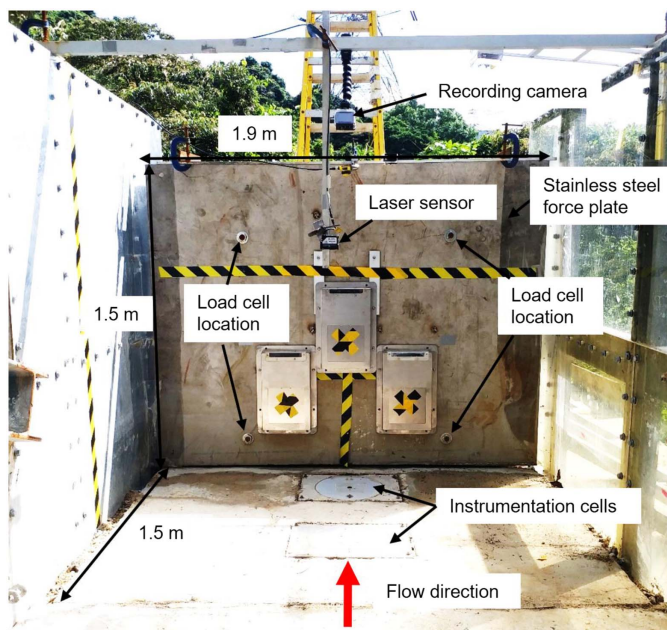


Fig. 2. Front view of L-shaped reinforced concrete barrier.

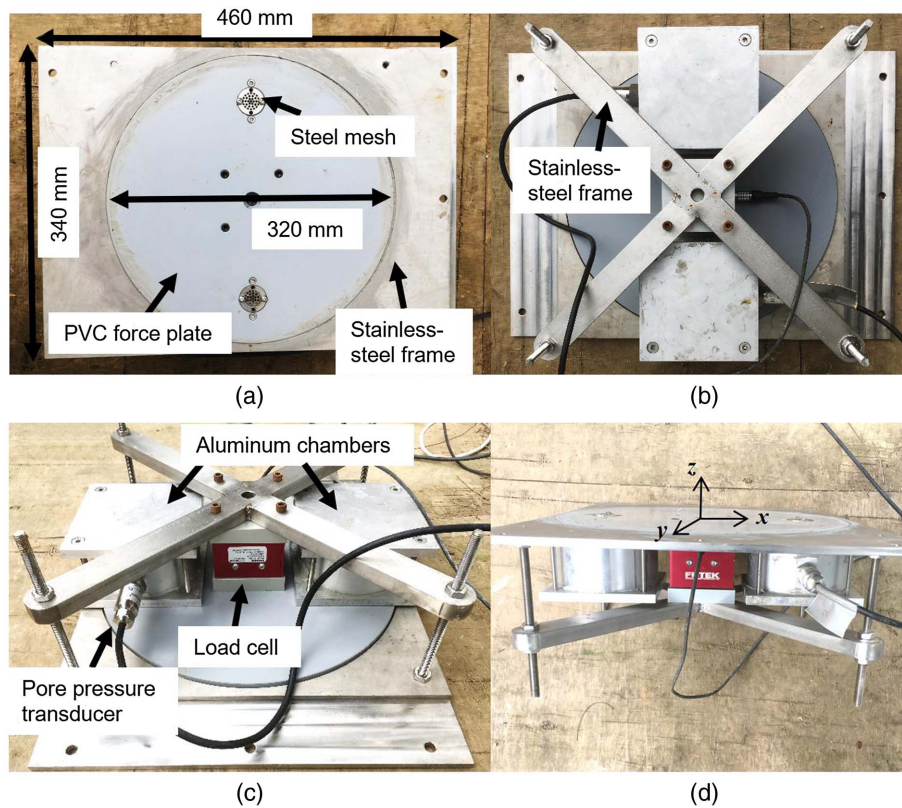


Fig. 3. Details of instrumentation cell: (a) top view; (b) bottom view; (c) bottom side view; and (d) top side view.

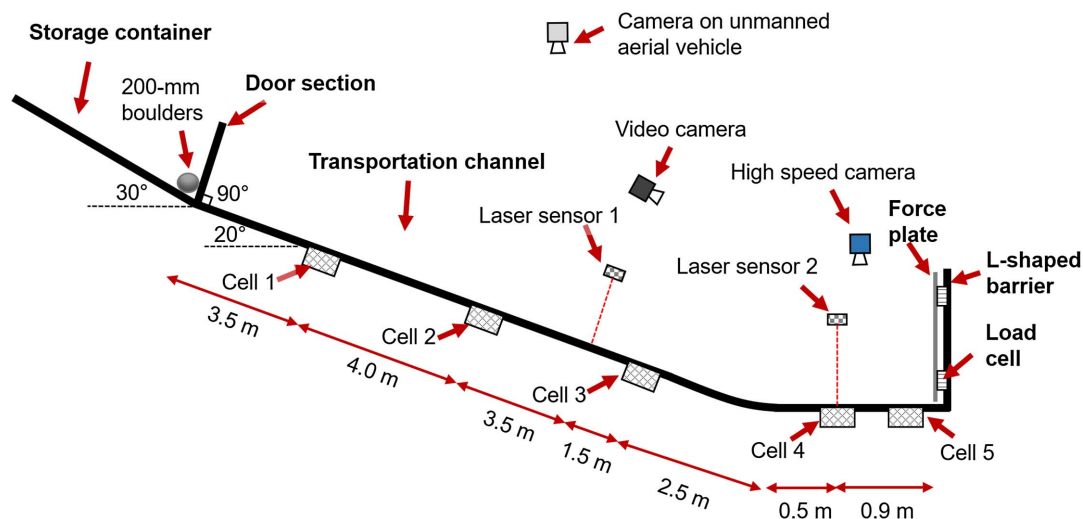


Fig. 4. Side schematic of test and instrumentation setup (not drawn to scale).

on a cross beam supported by the stainless steel frame [Fig. 3(b)]. The PVC plate had two openings with meshes (to filter fines) to enable the measurement of the changes in pore water pressure. Two cylindrical chambers constructed using aluminum with a diameter of 0.10 m and a height of 0.05 m were connected to each opening on the PVC plate. On the side of the cylindrical chambers, an opening was provided to connect pore pressure transducers to measure changes in pore pressure [Fig. 3(c)]. Before each test, each cylindrical chamber was filled with water. When debris flow passed over the PVC plates, basal stresses and excess pore pressures

generated by the debris flow were measured by each instrumentation cell.

Fig. 4 indicates a side schematic of the test setup. Five instrumentation cells (Cells 1–5) were installed at the base of the channel to measure the debris flow properties. A laser sensor was mounted above the center of Cell 4, and another laser sensor was installed 1.5 m upstream from the center of Cell 3. Four piezoresistive load cells were sandwiched between the force plate and the reinforced concrete L-shaped barrier to measure the total impact force exerted by the debris flow. A high-speed camera was installed

Table 1. Test program and results

Test ID	Debris volume (m ³)	Quantity of boulders	Initial debris density (kg/m ³)	Debris frontal velocity, v (m/s)	First boulder velocity, v_b (m/s)	Flow depth, h (mm)	Froude number, Fr	Peak impact force (kN)	K_c
D	2.5	0	1,960	5.2	—	50	7.4	4.9	—
DB10	2.5	10	1,960	5.5	7.5	50	7.9	27.1	0.04
B1	0	1	—	—	6.0	—	—	41.3	0.08
B10	0	10	—	—	7.1	—	—	71.5	0.11

Table 2. Debris composition

Material	Average diameter (mm)	Bulk density (kg/m ³)	Mass fraction by total weight (%)	Mass fraction by dry weight (%)	Volume (%)
Gravel	20	558	28	36	21
Sand	2	957	49	61	36
Clay	<0.006	43	2	3	2
Water	—	344	21	—	41
Total	—	1,960	100	100	100

on top of the L -shaped barrier that recorded images at 300 frames per second (fps) with a resolution of $2,336 \times 1,728$ pixels. The images were used to deduce the velocities of the flow and boulders before impact. Additionally, a video camera was installed above Cell 3. This video camera was installed facing the L -shaped barrier. The video camera recorded images at 120 fps with a resolution of $1,920 \times 1,080$ pixels. An unmanned aerial vehicle was used to capture a bird's eye view of the entire test to record images at 30 fps with a resolution of $1,920 \times 1,080$ pixels.

Test Program and Test Procedures

In total, four tests were conducted. A debris flow with a volume of 2.5 m^3 (test D) and the same volume of debris flow with ten boulders (test DB10) were modeled. Furthermore, tests with single and ten boulders were also conducted. The test program is summarized in Table 1.

The boulders in each test were placed at the base of the storage tank behind the gate. For the single boulder, the granite sphere was placed in the middle of the tank behind the gate. For ten boulders, the granite spheres were placed in a line at the base of the storage tank (Fig. 4). The boulders in this study were modeled using spherical granite with a diameter d of 200 mm. The debris material was composed of gravel, sand, clay, and water with volumetric fractions of 0.21, 0.36, 0.02, and 0.41, respectively. The gravel and sand had typical sizes of 20 mm and 2 mm, respectively. Kaolin clay with a particle size smaller than 0.006 mm was adopted. Details of the debris composition are summarized in Table 2.

Before each test, the debris material was well mixed by a truck mixer and transported into the storage container to reach the target volume. After the preparation of test material in the container, a data logger and cameras were triggered, and the mechanical arm was lifted to release the gate.

Flow Characterization

The Froude number (Fr) is the ratio between the inertial force and the gravitational force of the flow in a channel and is expressed as follows:

$$Fr = \frac{v}{\sqrt{gh \cos \theta}} \quad (7)$$

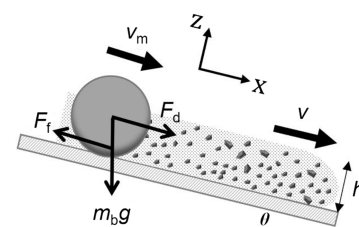
where g = gravitational acceleration (9.81 m/s^2 in this study) and θ = flume inclination (degrees). The Froude number has been recognized as a key parameter that governs the impact dynamics of open-channel flow (Hübl et al. 2009; Armanini et al. 2011; Choi et al. 2019). In this study, the Froude number of the flow before impacting the barrier ranges from 7.4 to 7.9, indicating that the inertial component is more dominant than the gravitational component of the flow; thus, dynamic loading is more significant (Faug 2015; Sovilla et al. 2016).

New Equation to Estimate Boulder Impact with Debris Cushioning

Debris flows arrested by a rigid barrier may act as a cushion to attenuate the impact energy of incoming boulders as the debris reflects from the barrier to the upstream direction. In this section, a new approach is proposed to predict the boulder impact force by explicitly considering the debris-boulder interaction.

Fig. 5 indicates a schematic of boulder motion in a debris flow. When a boulder is entrained in a flow, the boulder is subjected to a gravitational force, $m_b g$, frictional force between the boulder and the flow bed, F_f , and drag force from the flow, F_d . A mathematical equation to describe the boulder motion is expressed as follows:

$$\frac{dv_m}{dt} = g \sin \theta - \frac{F_f}{m_b} + \frac{F_d}{m_b} \quad (8)$$

**Fig. 5.** Side schematic of boulder motion in debris flow.

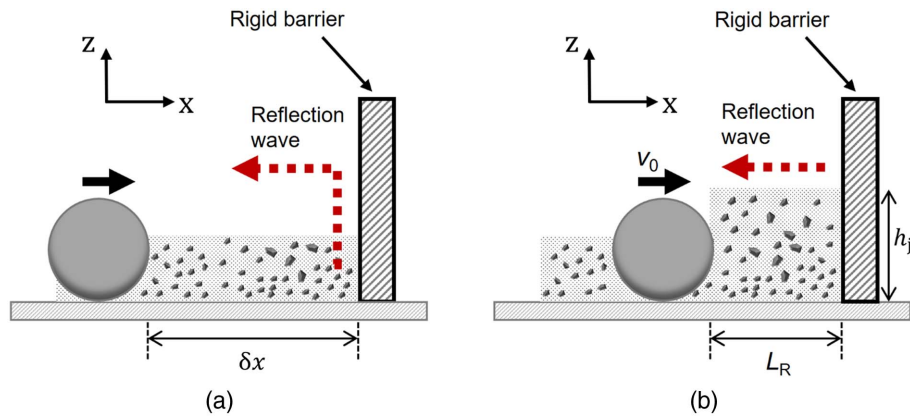


Fig. 6. Side schematic of boulder motion during debris flow impact: (a) debris front just reaches barrier location; and (b) boulder starts to interact with debris reflection wave.

where v_m = boulder velocity (m/s) during motion; and t = time (s) after the gate has been opened. By assuming mainly translational motion, the frictional force F_f can be simplified as follows:

$$F_f = \mu m_b g \cos \theta \quad (9)$$

where μ = interface friction coefficient between the boulder and the channel bed. Assuming that the boulder is fully submerged in the flow, the drag force F_d on the boulder is exerted by the flow and is proportional to the square of the relative velocity between the flow and the boulder (Alexander and Cooker 2016), which is expressed as follows:

$$F_d = \frac{1}{2} C_d A \rho \delta v^2 \quad (10)$$

where C_d = drag coefficient; A = cross-sectional area of the boulder in the plane perpendicular to the flow; ρ = flow density; and δv = relative velocity of the flow and the boulder. When the flow velocity v is larger than the boulder velocity v_m , the drag force is in the same direction as the flow. When the flow velocity v is smaller than the boulder velocity v_m , the drag force is opposite that of the flow direction. Substituting Eqs. (9) and (10), Eq. (8) can then be expressed as follows:

$$\frac{dv_m}{dt} = g \sin \theta - \mu g \cos \theta + \frac{C_d A \rho \delta v^2}{2m_b} \quad (11)$$

Eq. (11) neglects the force from the boulder-boulder interaction, which is reasonable for debris flows with a low boulder fraction. For flow that has a high boulder fraction, the interaction forces of boulder-boulder and boulder-flow should also be taken into account.

By obtaining the boulder velocity when impacting the barrier with Eq. (11), the boulder impact force can be calculated using the Hertz equation [Eqs. (2)–(6)]. The stainless steel force plate and granite boulders adopted in this study have Young's moduli of 200 GPa and 50 GPa, and Poisson's ratios of 0.3 and 0.2, respectively. Substituting the material properties into Eqs. (2)–(6) yields:

$$F_b = 6100 K_c v_b^{1.2} r_b^2 \quad (12)$$

The debris cushioning effect on boulder impact is mainly attributed to the attenuation of the boulder impact velocity, v_b . A reduced load reduction factor K_c can be expressed as follows:

$$K_c = 0.1 \left(\frac{v_b}{v_0} \right)^{1.2} \quad (13)$$

The boulder velocity attenuation by the arrested debris is schematically indicated in Figs. 6(a and b). Fig. 6(a) indicates a debris flow front just as it reaches the barrier. The relative distance between the debris flow and boulder fronts is given as δx . After the debris impacts the barrier, the arrested debris forms a reflection wave [Fig. 6(b)] with a height of h_j . This wave propagates in the upstream direction with a speed of v_r . Before impacting the barrier, the boulder first interacts with the reflection wave with length L_R [Fig. 6(b)], which serves as a cushioning thickness and dissipates the energy of the incoming boulder. The velocity of the boulder, v_b , when impacting the barrier is then reduced compared with its initial velocity, v_0 , before interacting with the reflection wave.

After the boulder enters into the reflection wave, the drag force, F_d , exerted by the flow can be calculated using Eq. (10). An assumption is made that the flow is uniform and homogeneous and that the motion of the boulder can be idealized as translational motion along a smooth channel bed. As the drag force from the flow becomes more significant than that of the frictional force from the flow bed, for simplicity, only the drag component is considered to influence the boulder velocity. The impact velocity of the boulder, v_b , is given as follows:

$$v_b = v_0 e^{-0.75 C_d \frac{\rho L_R}{\rho_b d}} \quad (14)$$

Substituting Eq. (14) into Eq. (13), the load reduction factor considering the cushioning effects provided by viscous damping can be expressed as follows:

$$K_c = 0.1 e^{-0.9 C_d \frac{\rho L_R}{\rho_b d}} \quad (15)$$

The drag coefficient C_d in Eqs. (14) and (15) can be taken as unity for a blunt body (Alexander and Cooker 2016). The boulder density ρ_b equals 2,800 kg/m³, which was obtained from the measured boulder mass. More details on Eq. (14) are given in the Appendix.

Interpretation of Test Results

Observed Flow Kinematics

The time history of the flow-front position has been adopted by Iverson et al. (2010) to describe the debris flow mobility. Fig. 7 indicates the time histories of the flow-front position of the boulders and debris flow as captured by the video camera mounted on the unmanned aerial vehicle. The flow-front position is characterized relative to the distance from the gate of the storage tank and is expressed as s . The acceleration of a point mass is indicated in Eq. (11). By neglecting the drag force, the theoretical flow distance s of a point mass can be expressed as follows:

$$s = \frac{g \sin \theta - \mu g \cos \theta}{2} t^2 \quad (16)$$

When flow is on the inclined portion of the channel, $\theta = 20^\circ$, and when flow is on the depositional area, $\theta = 0^\circ$. The test with a single boulder (test B1) and the test with ten boulders (test B10) had similar time histories of the flow-front position because the small amount of boulders induced insignificant boulder interactions. Considering a friction coefficient $\mu = 0.1$, Eq. (16) can well estimate the boulder motion in the pure boulder tests (tests B1 and B10). This implies that assuming a pure translational motion is not an unreasonable approach to idealize the boulder motion in this study.

The test with just debris flow (test D) and the test with a mixture of debris flow and boulders (test DB10) exhibited similar kinematics at the debris front. For both test D and test DB10, the debris fronts accelerated 0.5 s after the opening of the gate and achieved a nearly constant velocity of approximately 6 m/s along the inclined section of the channel. When the debris reached the end of the inclined section of the channel, and the flow decelerated by approximately 10% just before impacting the L -shaped barrier. The debris fronts for only debris flow (test D) and debris flow with ten boulders (test DB10) always remained ahead of flow fronts for pure boulder tests (tests B1 and B10) before impacting the barrier. This was because the debris front was driven by both its self-weight and the earth pressure in the flow direction (longitudinal direction) and can be quantified by a simplified depth-averaged momentum equation. The depth-averaged momentum equation was first proposed by Savage and Hutter (1989) and subsequently widely adopted to describe the motions of both dry granular flows (Gray et al. 1999; Gray and Ancey 2011) and debris flows (Iverson 1997; Iverson et al. 2010; Johnson et al. 2012; Iverson and George 2014). A simplified depth-averaged momentum equation can be expressed as follows:

$$\frac{du}{dt} = g \sin \theta - \mu g \cos \theta - k \frac{\partial h}{\partial x} g \cos \theta \quad (17)$$

where u = depth-averaged flow velocity (m/s) parallel to the channel bed; k = longitudinal earth pressure coefficient; and x = downslope distance (m). In Eq. (17), the term du/dt is the acceleration at an arbitrary location of the flow mass, $g \sin \theta$ represents the translational motion downslope, $\mu g \cos \theta$ represents the basal frictional resistance, and $k(\partial h/\partial x)g \cos \theta$ characterizes the longitudinal earth pressure within the flow mass. The term $k(\partial h/\partial x)g \cos \theta$ is negative within the head of the flow mass as the flow depth gradually decreases along the flow direction within the flow head. Therefore, the longitudinal earth pressure can increase the acceleration du/dt and accelerate the flow head, leading to a higher velocity than the boulders entrained in the flow. The flow distance for a frictionless point mass ($\mu = 0.0$) calculated by Eq. (16) is indicated in Fig. 7. The time history of this flow distance underestimates the

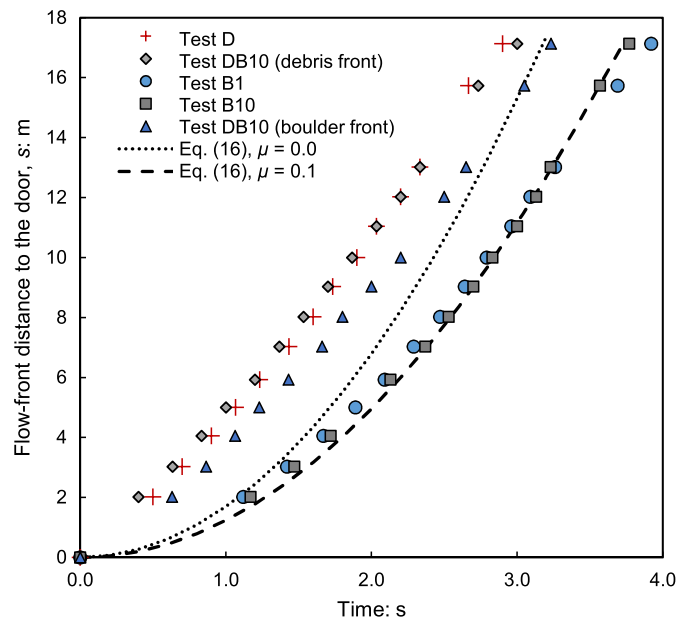


Fig. 7. Time histories of frontal position of boulders and debris flow.

measured motion of debris fronts for both the debris flow test (test D) and the test of debris flow with ten boulders (test DB10). The underestimation may be attributed to the larger longitudinal pressure compared with the basal friction, as expressed in Eq. (17). This caused a larger acceleration than the acceleration of a frictionless point mass $g \sin \theta$. Eq. (16) with $\mu = 0.0$ overestimates the motion of boulder front when there is no debris flow but underestimates the motion of the boulder front when the boulders are entrained in the debris flow. The overestimation may be mainly caused by the deceleration of the boulder motion due to basal friction. The underestimation may be mainly attributed to the acceleration of the boulder motion due to the drag force from the debris flow, as expressed in Eq. (11).

The movement of the boulders observed in this study was different from the kinematics of particle-size segregation (Jullien and Meakin 1990; Makse et al. 1997; Jing et al. 2017), whereby coarse particles usually segregate to the flow surface by kinetic sieving and are transported to the flow front by the shear stress of the flow (Johnson et al. 2012). In this study, the flow maintained a high pore pressure that liquefied the flow. Therefore, the flow cannot lift the boulders because the boulders were more than twice the flow depth, and the density of the boulder was 1.4 times the bulk density of the flow. The movement of the boulder was then dominated by the drag force of the flow on the boulders. Under this circumstance, when boulders are entrained by the debris flow along the flow path, the boulders may move slower than the debris front and impact the barrier after the debris front. The first arrested debris can then form a cushioning layer to dissipate the boulder energy before impact. To be noted is that the transportation distance of debris flow can also affect the process of particle-size segregation. With a much longer transportation distance in the field, coarse particles may tend to segregate to the flow front when flows are not liquefied (Zhang et al. 2011).

The high pore pressure maintained in the debris flows was mainly attributed to the clay content (Iverson 1997; Iverson et al. 2010). Fig. 8 provides a comparison of liquefaction ratio, which is the ratio between the pore water pressure u_w and the total normal stress σ , with different clay contents. The liquefaction ratios for pure debris flow (test D) and debris flow with ten boulders

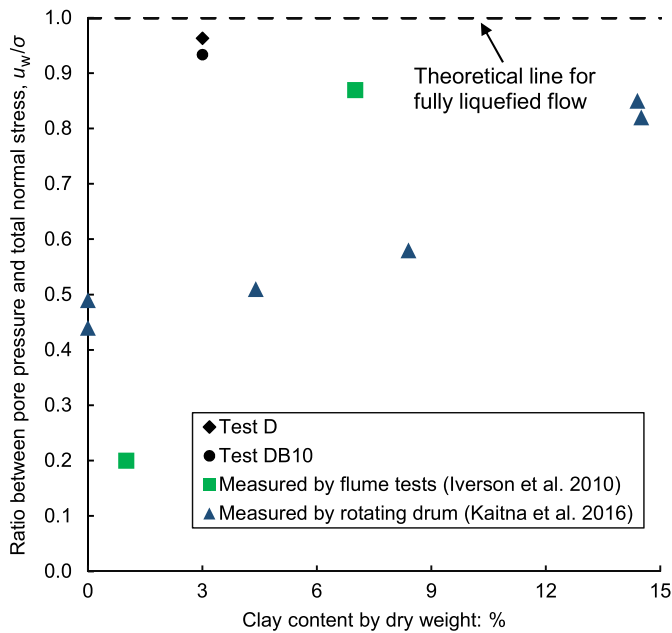


Fig. 8. Measured liquefaction ratio at different clay contents.

(test DB10) at the location of Cell 4, which was 0.9 m away from the force plate, were measured. The measured liquefaction ratios for both test D and test DB10 were close to unity, and pore water pressures were approximately 1.6 times that of hydrostatic conditions when the debris flows deposited behind the barrier. The high pore pressures mean that the flows were nearly liquefied, and the

grain contact stresses were minimal. Similarly, Iverson et al. (2010) reported that their flows remained liquefied even after deposition. Liquefied flows were especially pertinent for flows with high clay (particle size < 0.0625 mm) content. In contrast, flows with lower clay contents [less than or equal to 1% reported by Iverson et al. (2010)] resulted in higher effective stresses. Therefore, the clay content plays an important role in generating excess pore pressures in debris flows. Observations from vertically rotating drum tests by Kaitna et al. (2016) also indicated an increasing trend of the liquefaction ratio for steady-state flows with increasing clay content. The clay content in a debris flow maintains pore pressure by decreasing the permeability of the pore water. Decreased permeability can lead to an estimated time of 4,000 s to dissipate the pore pressure for a depth of 0.1 m (Major et al. 1997; Major 2000; Iverson et al. 2010). The liquefied flow conditions also imply that a hydraulic approach can be adopted to estimate the impact loads of the debris deposits.

Fig. 9 indicates the observed impact kinematics of only the debris flow (test D) and the debris flow with ten boulders (test DB10). When the debris flow impacted the barrier, the flow jumped along the face of the barrier [Fig. 9(a)] and was immediately reflected back upstream [Fig. 9(b)]. As the reflected wave propagated upstream [Fig. 9(c)], it interacted with the incoming flow that had not yet impacted the barrier. Eventually, the debris deposited and reached a static state with a horizontal surface [Fig. 9(d)]. The horizontal deposition profile implies that a zero deposition angle can be reached when debris flow is in a liquefied condition. For boulder-enriched debris flows, the debris front arrived at the barrier earlier than the boulders [Fig. 9(e)]. After the debris front impacted the barrier, the two boulders at the flow front impacted the barrier [Fig. 9(f)]. As more debris was arrested and reflected upstream

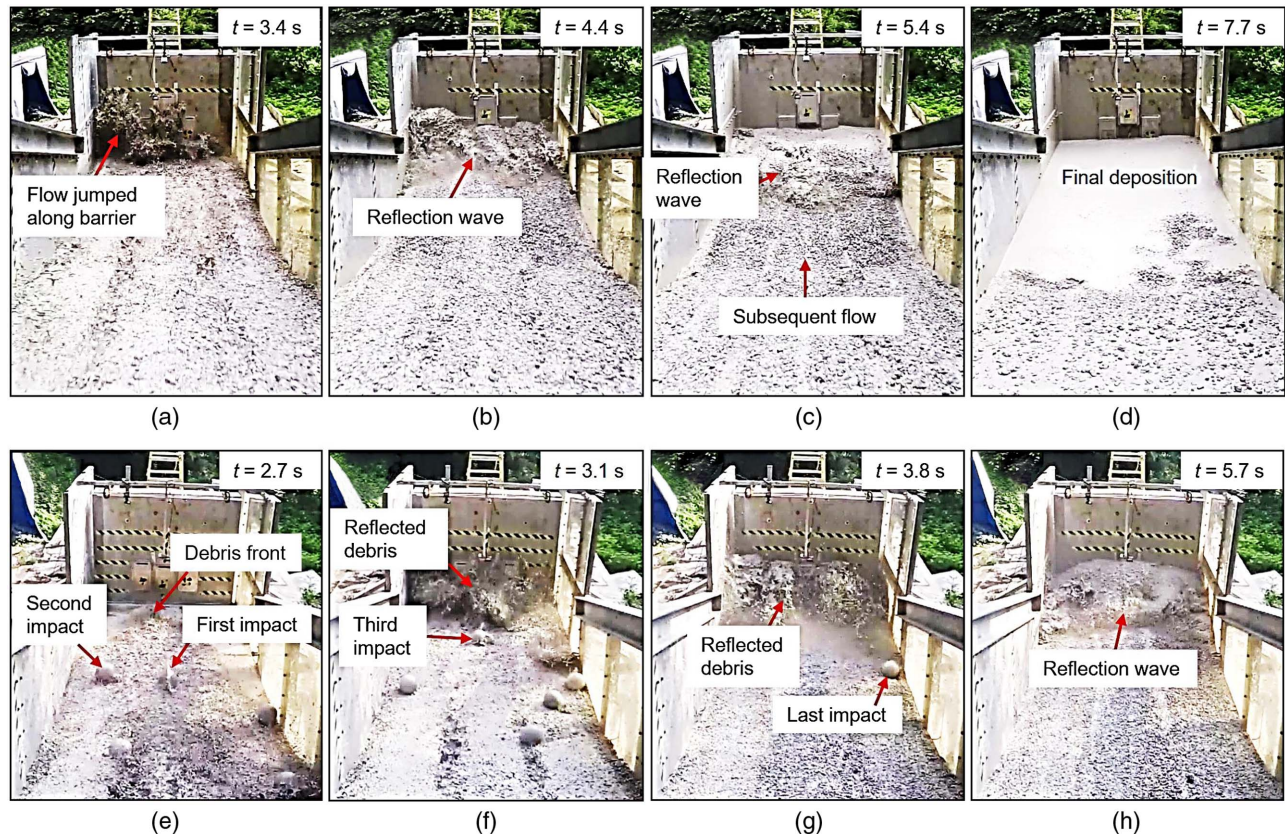


Fig. 9. (a)–(d) Observed impact kinematics of debris flow (test D); and (e)–(h) debris flow with ten boulders (test DB10).

by the barrier, incoming flow and boulders impacted the reflected debris flow [Figs. 9(f–h)]. In essence, the reflected debris flow provided a cushioning effect for incoming boulders. At the end of the impact process, all of the boulders were buried in the deposited debris material, and the same deposition profile as indicated in Fig. 9(d) was obtained. The observed kinematics of the boulder-enriched debris flows demonstrated that boulders may not necessarily be segregated to the flow front due to their much larger size than the flow depth and liquefied flow condition. The earlier arrested debris material by the barrier can form a cushioning layer through viscous damping, which dissipates the impact energy of the subsequent boulders.

Impact Force of Debris Flow

Fig. 10 provides a comparison of the time histories of the measured total impact force of debris flow (test D) and debris flow with ten boulders (test DB10). To examine the complex impact dynamics of boulder-enriched debris flows, we first look into the impact load exerted by only a debris flow. At $t = 3.0$ s, the debris impacted the barrier. The total force exerted on the barrier reached a peak load at $t = 4.4$ s. The total force gradually decreased until $t = 7.3$ s and reached a static state. The impact force is normalized by a theoretical impact force calculated by Eq. (1) with $\alpha = 1.0$. The density used to calculate the impact force is deduced from the measured peak normal stress and flow depth at Cell 3 (Fig. 4), which was located 4.4 m upstream from the barrier. The measured density was $1,870 \text{ kg/m}^3$, which was approximately 5% lower than the initial debris density ($1,960 \text{ kg/m}^3$). The impact velocity is taken as the average velocity of the flow front before impacting the barrier. The preimpact velocity was measured using the high-speed camera. The flow depth was measured using laser sensor 2 (Fig. 4) at the time that the flow impacts the barrier to avoid the influence of the reflected debris material. Given the accurate measurements of the flow density, impact velocity, and flow depth, the measured peak force is well-captured by the hydrodynamic equation when α is unity.

Higher α values are usually suggested by international design guidelines (Kwan 2012; Volkwein 2014; Vagnon and Segalini 2016) to consider the influence of hard inclusions and different debris flow types. However, the largest debris material particle in this study was only 20 mm, which did not induce obvious impulses. Moreover, measurements from the instrumentation cells in Fig. 8 indicate that the debris flow impact in this study was an undrained process due to the high rate of loading and low permeability of the debris material. The nearly liquefied state induces less energy dissipation during impact compared with that of dry granular flows, which readily dissipate flow kinetic energy as grains shear and the granular assembly compresses (Ng et al. 2017). The liquefied flow may also be the reason that an equivalent fluid approach is suitable for predicting the impact load of a debris flow. By treating debris flow that can maintain high excess pore pressure as an equivalent fluid, the major remaining challenge in estimating the impact load is the effects caused by the large and hard inclusions, which generate sharp impulses during impact.

Impact Force of Boulder-Enriched Debris Flow

The force-time history for debris flow with ten boulders (test DB10) indicates that the debris acted as a cushion for the boulders in the flow. Subsequent impulses generated from boulder impact were dampened as the volume of debris flow arrested by the barrier increased. The cushioning mechanism was caused by the viscous shear resistance between boulders and the pore fluid and the shear

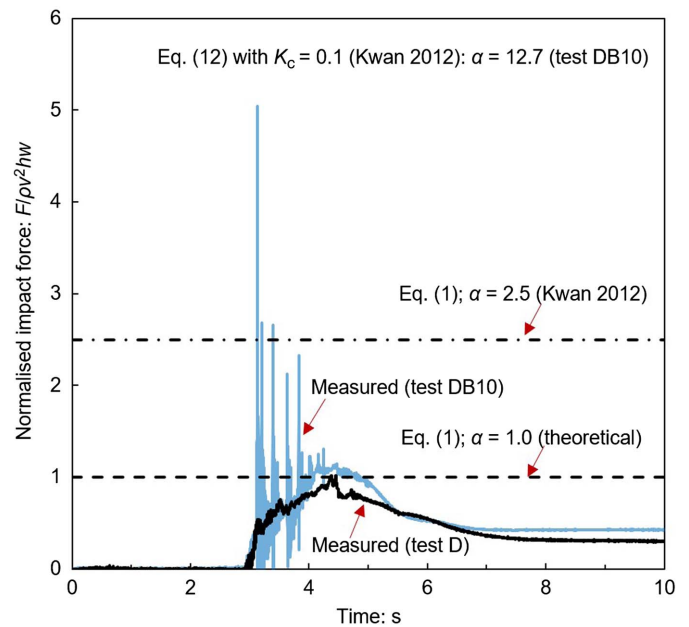


Fig. 10. Time histories of normalized impact force of debris flow (test D) and debris flow with ten boulders (test DB10).

resistance between the boulders and the finer solid particles in the debris flow. By comparing the time history of the pure debris flow impact with the boulder-enriched debris, sharp impulses were observed to be induced by the boulders. The peak load occurred at $t = 2.9$ s and was caused by a combination of the debris flow and boulder loadings. After the peak impulse occurred, four additional impulses with normalized impact forces ranging from 2.1 to 2.7 were caused by the other boulders in the flow. Additionally, impulses with normalized forces from 1.2 to 1.3 were observed from $t = 3.8$ s to $t = 4.1$ s. Decomposing the total impact force gives normalized boulder impact forces of approximately only 0.2 (from $t = 3.8$ s to $t = 4.1$ s). The normalized impact force from the debris increased until it reached a peak load, which was 1.1, at $t = 4.2$ s. Subsequently, the impact force decreased gradually until a static state was reached at $t = 7.1$ s.

The hydrodynamic impact model [Eq. (1)] with an α of 1.0 cannot capture the peak impulses from boulder impact but can still capture the peak load induced by the debris flow. By comparing the results predicted using Eq. (1) with an α of 2.5 (Kwan 2012), the peak load is still underestimated by more than 50%, bearing in mind that the recommended design value by Kwan (2012) considers hard inclusions in the debris flow. This is because the fundamental assumptions behind Eq. (1) and Eqs. (2)–(6) are different. The hydrodynamic equation treats the complex debris flow as an equivalent fluid (Hungry et al. 1984) that exerts a force distributed over a finite area. In contrast, the Hertz equation (Johnson 1985) assumes a concentrated elastic impact between a sphere and a plane over a very small contact area. Therefore, only significantly higher α values in the hydrodynamic equation can capture the effects of boulder impact—but it has practical limitations. The underestimation of the loading induced by boulder-enriched debris flow by Eq. (1) highlights the uncertainty in using α (Zhang 1993; Kwan 2012; Vagnon and Segalini 2016). For boulder-enriched debris flow, the hydrodynamic impact model should be used to estimate the debris impact force, whereas the Hertz equation still needs to be used to estimate the boulder impact force. A criterion that can distinguish between boulder and debris is recommended by

Song et al. (2018). They recommended a ratio of boulder diameter to flow depth, d/h , where particles with size $d/h \geq 0.6$ can be regarded as boulders. However, to determine the impact forces for boulder-enriched debris flow, a K_c value considering the effects of viscous damping of the debris flow can further optimize designs.

Performance of Newly Proposed Equation for Estimating Debris Cushioning on Boulder Impact

Fig. 11 indicates the load reduction factors, K_c , resulting from different lengths of debris reflection wave [Fig. 6(b)] normalized by boulder diameter, L_R/d . The length of the reflection wave serves as a cushioning thickness to dissipate boulder impact. The high-speed camera, which was mounted on top of the barrier (Fig. 4), was adopted to capture L_R and the velocities of the boulders on interacting with the reflection wave. The boulder impact forces for debris mixed with ten boulders (test DB10) are extracted from Fig. 10 by removing the loads induced from the debris and by only considering the transient impulses. The K_c values of the tests using a single boulder (test B1) and ten boulders (test B10) are indicated for comparison and are both found to be close to the recommended K_c value of 0.1 in the literature (Hung et al. 1984; VanDine 1996; Kwan 2012). This is because the lengths of the debris reflection wave equaled zero; thus, there was no cushioning effect from the debris. The measured K_c from the test with ten boulders without debris (test B10) is found to be 10% larger than the recommended design value of 0.1, which is attributed to two boulders impacting the barrier at almost the same time (impact interval was less than 0.03 s from the unmanned aerial vehicle images). The calculated $K_c = 0.11$ for the test with ten boulders without debris (test B10) implies that a higher than recommended K_c of 0.1 may be needed to account for the possible superposition of boulder impact loads when $L_R/d = 0$. Meanwhile, superposition of the debris flow impact load should also be carried out.

When $L_R/d > 0$, debris reflection was formed before a boulder impacted the barrier. K_c decreases sharply and keeps decreasing with an increasing L_R/d because more boulder energy was dissipated by the enlarging debris reflection wave. In addition, L_R/d values from 0.4 to 2.0 lead to a K_c that is as much as 80% lower

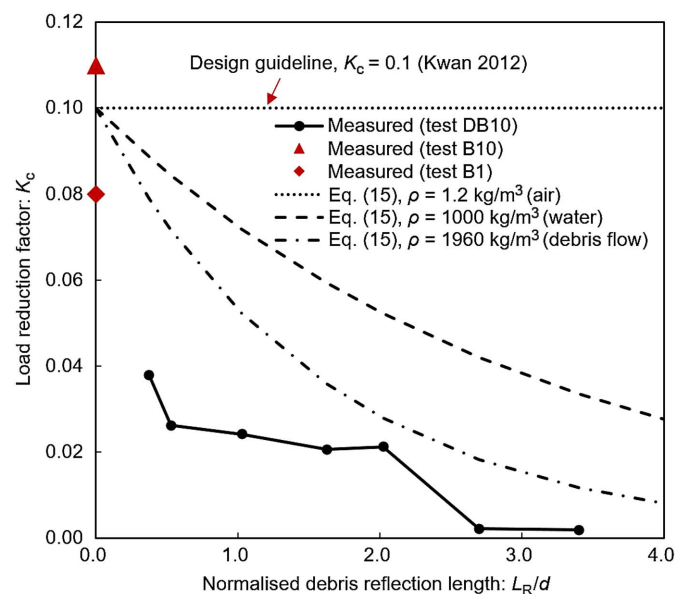


Fig. 11. Comparison of load reduction factor against normalized debris reflection length.

than the K_c of 0.1. At a distance of $L_R/d \geq 2.7$, K_c is approximately zero. Evidently, the length of the debris reflection wave contributes to attenuating the boulder impact force.

Calculated K_c values using Eq. (15) as a function of the normalized debris reflection length, L_R/d , are indicated. K_c values are significantly affected by the flow density. When the flow is considered to be air (dry granular flow), the calculated K_c value equals the suggested value by the design guideline (Kwan 2012). A flow density equal to that of pure water may overly estimate the K_c values. By applying a flow density of $1,960 \text{ kg/m}^3$, which was the initial debris flow density, Eq. (15) can reasonably estimate the load reduction factor K_c and provide an upper bound for the measured K_c . Overestimating K_c may occur because Eq. (15) simplifies the debris reflection as a uniform and homogenous fluid and neglects the interaction between the boulder and the debris solid fraction, which is approximately 60% of the total flow volume. In addition, only the drag force is considered by Eq. (15) for cushioning the boulder impact. However, cushioning material in front of the rigid barrier has been reported to change the load spreading process, which further attenuates the load transmitted to the barrier (Ng et al. 2018; Su et al. 2019). Nevertheless, Eq. (15) well estimates the decreasing trend of K_c with an increase in the reflection wave length and is capable of providing a first approximation of K_c to quantify the cushioning effect from viscous damping.

To be noted is that spherical boulders with a uniform diameter were adopted in this study to easily characterize boulder kinematics and dynamics without the influence of different boulder sizes and shapes. The proposed Eq. (15) assumes that the diameter of the boulder d is smaller than the thickness of the reflection wave h_j , as indicated in Fig. 6(b). The proposed Eq. (15) is expected to hold for boulders with a diameter $d < h_j$ because this diameter is consistent with the assumptions made by Eq. (15). Song et al. (2018) recommended that Eqs. (2)–(6) should be adopted to estimate the boulder impact force for boulders with a diameter larger than 0.6 times the flow depth h . Therefore, a boulder with a diameter $0.6h < d < h_j$ is recommended for adopting Eq. (15). For a small boulder with a size approaching 0, the L_R/d approaches infinity, the cushioning effect of the reflected debris on the boulder is very significant, and the boulder impact force can be neglected. For this condition, K_c equals 0, as calculated by Eq. (15). The impact force of the debris flow can be calculated by using only the continuum approach, such as the hydrodynamic equation [Eq. (1)]. For a boulder with a diameter larger than h_j , the effects of viscous damping may be reduced due to the smaller contact area than the area when a boulder is fully immersed in the flow. Notwithstanding, a $K_c = 0.1$ would still be adopted to provide a conservative prediction. When $d \gg L_R$ and L_R/d approaches 0, the cushioning effect from the reflected debris can be neglected due to the negligible cushioning thickness, and K_c should be taken as 0.1 to estimate the boulder impact force in a debris flow.

The proposed Eq. (15) does not consider the effects of the number of boulders on the load reduction factor K_c . In this study, the performance of Eq. (15) is only verified by debris flow that entrained ten spherical boulders with a boulder fraction of up to 2% of the debris flow volume. For debris flows with a much larger number of boulders and a much higher boulder fraction, the frictional and collisional stresses among boulders may be more prominent than the damping provided by the debris flow. Therefore, the proposed equation may need to be modified for a much higher boulder fraction. A further investigation of the effects of boulder fractions on the impact dynamics of boulder-enriched debris flow is still warranted.

In this study, the Hertz model, together with an empirical coefficient that implicitly considers plastic deformation, was adopted to

estimate the boulder impact force. Worth mentioning is that analytical models exist that can explicitly consider the plastic deformation during boulder impact (Yigit et al. 2011; Brake 2012; Ma and Liu 2015). These methods usually require information on the evolution of the plastic regions (Ma and Liu 2015). However, the difficulty in measuring such data has hindered a well-accepted approach that considers plastic deformation. Wang et al. (2020) summarized 18 theoretical elastoplastic contact models and found that the definition of the yield condition during the loading phase is necessary for an accurate prediction of the impact. Evidently, further investigation of the yield criterion for a boulder impact on barriers would enhance a more rational approach for estimating the boulder impact force. Nevertheless, the more pragmatic engineering approach with an empirical coefficient K_c as expressed in Eqs. (2)–(6) has the merit of being simple and robust enough for an engineering design and is currently widely adopted in engineering practice internationally (SWCB 2005; NILIM 2007; Kwan 2012).

Implications for Designing Debris-Resisting Barriers in Practice

The impact dynamics of debris flow against debris-resisting barriers are not well understood because of the heterogeneous nature of debris flows and the idiosyncrasies of the natural settings involved. Therefore, to ensure a conservative barrier design, the aforementioned factors should be considered. To highlight the general dearth of knowledge in estimating boulder impact, an empirical load reduction factor of 0.1 is required to reduce the impact load predicted using the elastic Hertz equation [Eq. (12)]. Kwan (2012) suggested that if simultaneous boulder impact may occur, the design impact load per meter run of the barrier should be taken as the impact load of the largest boulder divided by the boulder diameter. Following this approach, the total design impact load for the rigid barrier is 650 kN, which is 23 times higher than the measured peak impact load for the debris flow with ten boulders from the physical experiments in this study (Fig. 10; test DB10). Evidently, room exists to enhance our understanding and to optimize the current design load of boulder-enriched debris flows.

Aside from the complexities attributed to the debris flow itself and the natural terrain, different types of debris-resisting barriers may also result in entirely different impact processes and dynamics. The results in this study are for a fully closed rigid barrier without overflow or barrier deformation. For open structures, such as baffles (Choi et al. 2015; Law et al. 2015; Ng et al. 2015) and slit dams (Choi et al. 2016; Zhou et al. 2020), debris may discharge through and around these structures, and the cushioning effect identified in this study may not be as prominent as that for closed barriers. For flexible barriers (Wendeler and Volkwein 2015; Wendeler et al. 2019; Song et al. 2019), the deformation of the barrier may lead to a different debris reflection compared with rigid barriers and alter the boulder-flow-barrier interaction process. To further rationalize the design of debris-resisting barriers in practice, advanced numerical modeling methods together with high quality physical data can potentially optimize the resisting capacity required by a barrier.

In engineering design practice, well-calibrated numerical models are utilized to optimize designs. For instance, a depth-averaged continuum numerical software 2d-DMM (Kwan and Sun 2006; Law and Ko 2018) and a finite element software package LS-DYNA have been recommended by design guidelines (Kwan 2012; Koo 2017) to obtain the design velocity and flow depth to estimate impact loads. Koo (2017) also recommended the use of

the LS-DYNA to model the impact dynamics of flow against rigid (Ng et al. 2018) and flexible (Koo and Kwan 2014; Cheung et al. 2018) barriers. Although LS-DYNA can also model boulder impact (Koo and Kwan 2014; Ng et al. 2018), a deficiency in the unique, reliable, and large-scale data has hindered the model calibration. The findings from this study stress the importance of modeling the interaction between debris and boulder for the barrier design. More recently, coupled approaches using the discrete element method with computational fluid dynamics have been reported (Li and Zhao 2018). However, the computational cost for such an approach limits its use for larger-scale problems in a practical engineering design. The observed importance of separately capturing the boulder and debris loads in this study further suggests that more advanced numerical approaches are needed to advance the state-of-the-art and rationalize the design of debris-resisting barriers.

Conclusions

A series of 28-m-long flume tests has been conducted to highlight the interaction between the debris flow and boulders on the impact behavior against rigid barriers. The results from this study were based on a debris flow mixture of gravel, sand, clay, and water with volumetric fractions of 0.21, 0.36, 0.02, and 0.41, respectively. The gravel and sand had average sizes of 20 mm and 2 mm, respectively. The clay had a particle size smaller than 0.006 mm. Boulders adopted by this study were spherical granite with a uniform diameter of 200 mm. The findings from this study may be described as follows:

1. Contrary to existing design practice where the boulder and debris impact loads are added to each other, the debris provides a cushioning effect to attenuate the impact force of the boulders.
2. For situations in which the debris flow front impacts the rigid barrier prior to boulders coming behind, the reflection wave of the debris flow propagates upstream after the debris front interacts with the barrier and provides a cushioning effect on the boulders. The enlarging reflection wave length could serve as a cushioning thickness with a length scale of L_R/d , where L_R = reflection wave length on interacting with each boulder and d = boulder diameter. The measured boulder impact loads in this study indicate that L_R/d values from 0.4 to 2.0 can reduce the impact load by up to 80% compared with existing design practice ($K_c = 0.1$), and $L_R/d \geq 2.7$ can lead K_c approximately to zero.
3. A new equation has been proposed and evaluated to estimate the K_c values with consideration of debris cushioning effects based on different L_R/d ratios. The new equation can serve as a scientific basis for optimizing design impact load for debris flow with a boulder fraction of up to 2% of the flow volume.

Appendix. Derivation of Eq. (14)

The boulder is assumed to be only subjected to the drag force [Eq. (10)] after the boulder enters into the reflection wave [Fig. 6(b)]. The acceleration of the boulder can be expressed as follows:

$$a(t) = -\frac{C_d A \rho \delta v^2}{2m_b} \quad (18)$$

The mass of the spherical boulders as a function of the boulder cross-sectional area A can be expressed as follows:

$$m_b = \frac{2}{3} \rho_b d A \quad (19)$$

Assuming that the flow velocity inside the reflection wave is zero, then the relative velocity of boulder and flow, δv , can be represented by the boulder velocity as a function of time, which is $\delta v = v(t)$. The boulder velocity, $v(t)$, after the boulder enters into the debris can be expressed as follows:

$$v(t) = v_0 + \int_0^t a(t) dt = v_0 - \frac{3C_d A \rho}{4\rho_b d} \int_0^t v^2(t) dt \quad (20)$$

As indicated in Fig. 6(b), the transportation distance of the boulder from entering into the reflection wave to impacting the barrier is L_R , which can be obtained by integrating the $v(t)$ indicated as follows:

$$L_R = \int_0^t v(t) dt \quad (21)$$

Solve Eq. (20) by taking the time derivative for both sides of the equation. With a boundary condition $v(0) = v_0$, substituting the resulting $v(t)$ into Eq. (21) yields Eq. (14).

Data Availability Statement

All data, models, or code that support the findings of this study are available from the corresponding author on reasonable request.

Acknowledgments

The work described in this paper was supported by a grant from the National Natural Science Foundation of China (51709052) and financial sponsorships from the Research Grants Council of the Hong Kong Special Administrative Region, China (Project Nos. AoE/E-603/18, T22-603/15-N, 16212618, and 16209717). This paper is published with the permission of the Director of Civil Engineering and Development and the Head of the Geotechnical Engineering Office of the Hong Kong Special Administrative Region of China.

References

- Alexander, J., and M. J. Cooker. 2016. "Moving boulders in flash floods and estimating flow conditions using boulders in ancient deposits." *Sedimentology* 63 (6): 1582–1595. <https://doi.org/10.1111/sed.12274>.
- Armanini, A., M. Larcher, and M. Odorizzi. 2011. "Dynamic impact of a debris flow front against a vertical wall." In *Proc., 5th Int. Conf. on Debris-Flow Hazards Mitigation: Mechanics, Prediction and Assessment*, 1041–1049. Rome: Casa Editrice Universita La Sapienza.
- Brake, M. 2012. "An analytical elastic-perfectly plastic contact model." *Int. J. Solids Struct.* 49 (22): 3129–3141. <https://doi.org/10.1016/j.ijsolstr.2012.06.013>.
- Cheung, A. K. C., J. Yiu, H. W. K. Lam, and E. H. Y. Sze. 2018. "Advanced numerical analysis of landslide debris mobility and barrier interaction." *HKIE Trans.* 25 (2): 76–89. <https://doi.org/10.1080/1023697X.2018.1462106>.
- Choi, C. E., G. Goodwin, C. W. W. Ng, D. K. H. Cheung, J. S. H. Kwan, and W. K. Pun. 2016. "Coarse granular flow interaction with slit-structures." *Geotech. Lett.* 6 (4): 1–8. <https://doi.org/10.1680/jgele.16.00103>.
- Choi, C. E., C. W. W. Ng, H. Liu, and Y. Wang. 2019. "Interaction between dry granular flow and rigid barrier with basal clearance: Analytical and physical modelling." *Can. Geotech. J.* 57 (2): 236–245. <https://doi.org/10.1139/cgj-2018-0622>.
- Choi, C. E., C. W. W. Ng, D. Song, R. P. H. Law, J. S. H. Kwan, and K. K. S. Ho. 2015. "Computational investigation of baffle configuration on impedance of channelized debris flow." *Can. Geotech. J.* 52 (2): 182–197. <https://doi.org/10.1139/cgj-2013-0157>.
- Faug, T. 2015. "Depth-averaged analytic solutions for free-surface granular flows impacting rigid walls down inclines." *Phys. Rev. E* 92 (6): 062310. <https://doi.org/10.1103/PhysRevE.92.062310>.
- Gray, J. M. N. T., and C. Ancey. 2011. "Multi-component particle-size segregation in shallow granular avalanches." *J. Fluid Mech.* 678: 535–588. <https://doi.org/10.1017/jfm.2011.138>.
- Gray, J. M. N. T., M. Wieland, and K. Hutter. 1999. "Gravity driven free surface flow of granular avalanches over complex basal topography." *Proc. R. Soc. A* 455 (1985): 1841–1874. <https://doi.org/10.1098/rspa.1999.0383>.
- Hübl, J., J. Suda, D. Proske, R. Kaitna, and C. Scheidl. 2009. "Debris flow impact estimation." In *Proc., 11th Int. Symp. on Water Management and Hydraulic Engineering*, 1–5. Skopje, Macedonia: Univ. of Ss. Cyril and Methodius.
- Hungr, O. 1995. "A model for the runout analysis of rapid flow slides, debris flows, and avalanches." *Can. Geotech. J.* 32 (4): 610–623. <https://doi.org/10.1139/t95-063>.
- Hungr, O., G. C. Morgan, and R. Kellerhals. 1984. "Quantitative analysis of debris torrent hazards for design of remedial measures." *Can. Geotech. J.* 21 (4): 663–677. <https://doi.org/10.1139/t84-073>.
- Iverson, R. M. 1997. "The physics of debris flows." *Rev. Geophys.* 35 (3): 245–296. <https://doi.org/10.1029/97RG00426>.
- Iverson, R. M. 2015. "Scaling and design of landslide and debris-flow experiments." *Geomorphology* 244 (Sep): 9–20. <https://doi.org/10.1016/j.geomorph.2015.02.033>.
- Iverson, R. M., and D. L. George. 2014. "A depth-averaged debris-flow model that includes the effects of evolving dilatancy. I. Physical basis." *Proc. R. Soc. A* 470 (2170): 20130819. <https://doi.org/10.1098/rspa.2013.0819>.
- Iverson, R. M., M. Logan, R. G. LaHusen, and M. Berti. 2010. "The perfect debris flow: Aggregated results from 28 large-scale experiments." *J. Geophys. Res.* 115 (3): F03005. <https://doi.org/10.1029/2009JF001514>.
- Jing, L., C. Y. Kwok, and Y. F. Leung. 2017. "Micromechanical origin of particle size segregation." *Phys. Rev. Lett.* 118 (11): 118001. <https://doi.org/10.1103/PhysRevLett.118.118001>.
- Johnson, C. G., B. P. Kokelaar, R. M. Iverson, M. Logan, R. G. LaHusen, and J. M. N. T. Gray. 2012. "Grain-size segregation and levee formation in geophysical mass flows." *J. Geophys. Res. Earth Surf.* 117 (F1): F01032. <https://doi.org/10.1029/2011JF002185>.
- Johnson, K. L. 1985. *Contact mechanics*. London: Cambridge University Press.
- Jullien, R., and P. Meakin. 1990. "A mechanism for particle size segregation in three dimensions." *Nature* 344 (6265): 425–427. <https://doi.org/10.1038/344425a0>.
- Kaitna, R., M. C. Palucis, B. Yohannes, K. M. Hill, and W. E. Dietrich. 2016. "Effects of coarse grain size distribution and fine particle content on pore fluid pressure and shear behavior in experimental debris flows." *J. Geophys. Res. Earth Surf.* 121 (2): 415–441. <https://doi.org/10.1002/2015JF003725>.
- Koo, R. C. H. 2017. *3D debris mobility assessment using LS-DYNA*. GEO Rep. No. 325. Hong Kong: Geotechnical Engineering Office, The HKSAR Government.
- Koo, R. C. H., and J. S. H. Kwan. 2014. *A numerical study of dynamic responses of two selected flexible rockfall barriers subject to punching and areal loads*. Technical Note No. TN 4/2014. Hong Kong: Geotechnical Engineering Office, The HKSAR Government.
- Kwan, J. S. H. 2012. *Supplementary technical guidance on design of rigid debris resisting barriers*. Technical Note No. TN 2/2012. Hong Kong: Geotechnical Engineering Office, The HKSAR Government.
- Kwan, J. S. H., and H. W. Sun. 2006. "An improved landslide mobility model." *Can. Geotech. J.* 43 (5): 531–539. <https://doi.org/10.1139/t06-010>.
- Lam, C., J. S. H. Kwan, Y. Su, C. E. Choi, and C. W. W. Ng. 2018. "Performance of ethylene-vinyl acetate foam as cushioning material for rigid debris-resisting barriers." *Landslides* 15 (9): 1779–1786. <https://doi.org/10.1007/s10346-018-0987-z>.

- Law, R. P. H., C. E. Choi, and C. W. W. Ng. 2015. "Discrete-element investigation of influence of granular debris flow baffles on rigid barrier impact." *Can. Geotech. J.* 53 (1): 179–185. <https://doi.org/10.1139/cgj-2014-0394>.
- Law, R. P. H., and F. W. Y. Ko. 2018. *Validation of geotechnical computer program "2d-DMM (Version 2.0)"*. GEO Rep. No. 332. Hong Kong: Geotechnical Engineering Office, The HKSAR Government.
- Li, X., and J. Zhao. 2018. "A unified CFD-DEM approach for modeling of debris flow impacts on flexible barriers." *Int. J. Numer. Anal. Methods Geomech.* 42 (14): 1643–1670. <https://doi.org/10.1002/nag.2806>.
- Lo, D. O. K. 2000. *Review of natural terrain landslide debris-resisting barrier design*. GEO Rep. No. 104. Hong Kong: Geotechnical Engineering Office, The HKSAR Government.
- Ma, D., and C. Liu. 2015. "Contact law and coefficient of restitution in elastoplastic spheres." *J. Appl. Mech.* 82 (12): 121006. <https://doi.org/10.1115/1.4031483>.
- Major, J. J. 1997. "Depositional processes in large-scale debris-flow experiments." *J. Geol.* 105 (3): 345–366. <https://doi.org/10.1086/515930>.
- Major, J. J. 2000. "Gravity-driven consolidation of granular slurries: Implications for debris-flow deposition and deposit characteristics." *J. Sediment. Res.* 70 (1): 64–83. <https://doi.org/10.1306/2DC408FF-0E47-11D7-8643000102C1865D>.
- Makse, H. A., S. Havlin, P. R. King, and H. E. Stanley. 1997. "Spontaneous stratification in granular mixtures." *Nature* 386 (6623): 379–382. <https://doi.org/10.1038/386379a0>.
- Ng, C. W. W., C. E. Choi, D. Song, J. S. H. Kwan, R. C. H. Koo, H. Y. K. Shiu, and K. K. S. Ho. 2015. "Physical modelling of baffles influence on landslide debris mobility." *Landslides* 12 (1): 1–18. <https://doi.org/10.1007/s10346-014-0476-y>.
- Ng, C. W. W., C. E. Choi, A. Y. Su, J. S. H. Kwan, and C. Lam. 2016. "Large-scale successive impacts on a rigid barrier shielded by gabions." *Can. Geotech. J.* 53 (10): 1688–1699. <https://doi.org/10.1139/cgj-2016-0073>.
- Ng, C. W. W., D. Song, C. E. Choi, J. S. H. Kwan, R. C. H. Koo, and W. K. Pun. 2017. "Impact mechanisms of granular and viscous flows on rigid and flexible barriers." *Can. Geotech. J.* 54 (2): 188–206. <https://doi.org/10.1139/cgj-2016-0128>.
- Ng, C. W. W., A. Y. Su, C. E. Choi, C. Lam, J. S. H. Kwan, R. Chen, and H. Liu. 2018. "Comparison of cushion mechanisms between cellular glass and gabions subjected to successive boulder impacts." *J. Geotech. Geoenviron. Eng.* 144 (9): 04018058. [https://doi.org/10.1061/\(ASCE\)GT.1943-5606.0001922](https://doi.org/10.1061/(ASCE)GT.1943-5606.0001922).
- NILIM (Natural Institute for Land and Infrastructure Management). 2007. *Manual of technical standard for establishing Sabo master plan for debris flow and driftwood*. [In Japanese.] Technical Note of NILIM No. 364. Tokyo: NILIM, Ministry of Land, Infrastructure and Transport.
- Savage, S. B., and K. Hutter. 1989. "The motion of a finite mass of granular material down a rough incline." *J. Fluid Mech.* 199: 177–215. <https://doi.org/10.1017/S0022112089000340>.
- Song, D., C. E. Choi, C. W. W. Ng, G. G. Zhou, J. S. Kwan, H. Y. Sze, and Y. Zheng. 2019. "Load-attenuation mechanisms of flexible barrier subjected to bouldery debris flow impact." *Landslides* 16 (12): 2321–2334. <https://doi.org/10.1007/s10346-019-01243-2>.
- Song, D., C. E. Choi, G. G. D. Zhou, J. S. H. Kwan, and H. Y. Sze. 2018. "Impulse load characteristics of bouldery debris flow impact." *Géotech. Lett.* 8 (2): 111–117. <https://doi.org/10.1680/jgele.17.00159>.
- Song, D., C. W. W. Ng, C. E. Choi, G. G. D. Zhou, J. S. H. Kwan, and R. C. H. Koo. 2017. "Influence of debris flow solid fraction on rigid barrier impact." *Can. Geotech. J.* 54 (10): 1421–1434. <https://doi.org/10.1139/cgj-2016-0502>.
- Sovilla, B., T. Faug, A. Köhler, D. Baroudi, J. T. Fischer, and E. Thibert. 2016. "Gravitational wet avalanche pressure on pylon-like structures." *Cold Regions Sci. Technol.* 126 (Jun): 66–75. <https://doi.org/10.1016/j.coldregions.2016.03.002>.
- Su, Y., Y. Cui, C. W. W. Ng, C. E. Choi, and J. S. H. Kwan. 2019. "Effects of particle size and cushioning thickness on the performance of rock-filled gabions used in protection against boulder impact." *Can. Geotech. J.* 56 (2): 198–207. <https://doi.org/10.1139/cgj-2017-0370>.
- Sun, H. W., T. T. M. Lam, and H. M. Tsui. 2005. *Design basis for standardised modules of landslide debris-resisting barriers*. GEO Rep. No. 174. Hong Kong: Geotechnical Engineering Office, The HKSAR Government.
- SWCB (Soil and Water Conservation Bureau). 2005. *Manual of soil and water conservation*. [In Chinese.] Nantou, Taiwan: SWCB.
- Vagnon, F., and A. Segalini. 2016. "Debris flow impact estimation on a rigid barrier." *Nat. Hazards Earth Syst. Sci.* 16 (7): 1691–1697. <https://doi.org/10.5194/nhess-16-1691-2016>.
- VanDine, D. F. 1996. *Debris flow control structures for forest engineering*. Clearwater, BC, Canada: Ministry of Forests.
- Volkwein, A. 2014. *Flexible debris flow barriers: Design and application: WSL Berichte, 18*. Birmensdorf, Switzerland: Swiss Federal Institute for Forest, Snow and Landscape Research WSL.
- Wang, H., X. Yin, H. Hao, W. Chen, and B. Yu. 2020. "The correlation of theoretical contact models for normal elastic-plastic impacts." *Int. J. Solids Struct.* 182–183 (Jan): 15–33. <https://doi.org/10.1016/j.ijssolstr.2019.07.018>.
- Wendeler, C., and A. Volkwein. 2015. "Laboratory tests for the optimization of mesh size for flexible debris-flow barriers." *Nat. Hazards Earth Syst. Sci.* 15 (12): 2597–2604. <https://doi.org/10.5194/nhess-15-2597-2015>.
- Wendeler, C., A. Volkwein, B. W. McArdell, and P. Bartelt. 2019. "Load model for designing flexible steel barriers for debris flow mitigation." *Can. Geotech. J.* 56 (6): 893–910. <https://doi.org/10.1139/cgj-2016-0157>.
- Yigit, A. S., A. P. Christoforou, and M. A. Majeed. 2011. "A nonlinear visco-elastoplastic impact model and the coefficient of restitution." *Nonlinear Dyn.* 66 (4): 509–521. <https://doi.org/10.1007/s11071-010-9929-6>.
- Zeng, C., P. Cui, Z. Su, Y. Lei, and R. Chen. 2015. "Failure modes of reinforced concrete columns of buildings under debris flow impact." *Landslides* 12 (3): 561–571. <https://doi.org/10.1007/s10346-014-0490-0>.
- Zhang, L. M., Y. Xu, R. Q. Huang, and D. S. Chang. 2011. "Particle flow and segregation in a giant landslide event triggered by the 2008 Wenchuan earthquake, Sichuan, China." *Nat. Hazards Earth Syst. Sci.* 11 (4): 1153–1162. <https://doi.org/10.5194/nhess-11-1153-2011>.
- Zhang, S. 1993. "A comprehensive approach to the observation and prevention of debris flows in China." *Nat. Hazards* 7 (1): 1–23. <https://doi.org/10.1007/BF00595676>.
- Zhou, G. G. D., J. Du, D. Song, C. E. Choi, H. S. Hu, and C. Jiang. 2020. "Numerical study on granular debris flow runoff against slit-dams by discrete element method." *Landslides* 17 (3): 585–595. <https://doi.org/10.1007/s10346-019-01287-4>.
- Zhou, G. G. D., D. Song, C. E. Choi, A. Pasuto, Q. C. Sun, and D. F. Dai. 2018. "Surge impact of granular flows: Effects of water content." *Landslides* 15 (4): 695–709. <https://doi.org/10.1007/s10346-017-0908-6>.